

# Journal of Geophysical Research: Solid Earth

## RESEARCH ARTICLE

10.1002/2017JB014524

**Key Points:**

- Array migration process can resolve the small-scale topographic variations on the mantle transition zone discontinuities
- A flat 410 coincides with the presence of a gap in the subducting plate at the top of the transition zone beneath eastern Java
- A positive temperature anomaly is likely responsible for our observation of an uplifted 660 beneath the Banda Sea

**Supporting Information:**

- Supporting Information S1
- Data Set S1

**Correspondence to:**

R. M. H. Dokht,  
ramin1@ualberta.ca

**Citation:**

Dokht, R. M. H., Gu, Y. J., & Sacchi, M. D. (2018). Migration imaging of the Java subduction zones. *Journal of Geophysical Research: Solid Earth*, 123.  
<https://doi.org/10.1002/2017JB014524>

Received 14 JUN 2017

Accepted 10 JAN 2018

Accepted article online 25 JAN 2018

## Migration Imaging of the Java Subduction Zones

**Ramin M. H. Dokht<sup>1,2</sup> , Yu Jeffrey Gu<sup>1</sup>, and Mauricio D. Sacchi<sup>1</sup>**

<sup>1</sup>Department of Physics, University of Alberta, Edmonton, Alberta, Canada, <sup>2</sup>Now at Pacific Geoscience Centre, Geological Survey of Canada, Natural Resources Canada, Sidney, British Columbia, Canada

**Abstract** Imaging of tectonically complex regions can greatly benefit from dense network data and resolution enhancement techniques. Conventional methods in the analysis of SS precursors stack the waveforms to obtain an average discontinuity depth, but smearing due to large Fresnel zones can degrade the fine-scale topography on the discontinuity. To provide a partial solution, we introduce a depth migration algorithm based on the common scattering point method while considering nonspecular diffractions from mantle transition zone discontinuities. Our analysis indicates that, beneath the Sunda arc, the depth of the 410 km discontinuity (the 410) is elevated by 30 km and the 660 km discontinuity (the 660) is depressed by 20–40 km; the region of the strongest anticorrelation is correlated with the morphology of the subducting Indo-Australian slab. In eastern Java, a “flat” 410 coincides with a documented slab gap, showing length scales greater than 400 km laterally and 200 km vertically. This observation could be explained by the arrival of a buoyant oceanic plateau at the Java trench at approximately 8 Ma ago, which may have caused a temporary cessation of subduction and formed a tear in the subducting slab. Our results highlight contrasting depths of the 410 and 660 along the shallow-dipping slab below the Banda trench. The 660, however, becomes significantly uplifted beneath the Banda Sea, which is accompanied by enhanced reflection amplitudes. We interpret these observations as evidence for a subslab low-velocity zone, possibly related to the lower mantle upwelling beneath the subducting slab.

### 1. Introduction

The Sunda trench, located in southeastern (SE) Asia, is an active convergent plate margin marked by the subduction of the Indo-Australian oceanic lithosphere (slab) beneath the Eurasian plate (Bird, 2003; Curran et al., 1979; Simons et al., 2007). The trench extends along strike for over 5,000 km from the Andaman Islands to the west of the active Banda arc (Widiyantoro et al., 2011a), which is identifiable by its 180° curvature resulting from the collision between the northward migrating Australian continental plate and the arc in the Early Pliocene (Katili, 1975; Spakman & Hall, 2010). The estimated age of the subducting oceanic lithosphere varies along the trench and decreases from the Late Jurassic (134–154 Ma) in southern Sumatra to the Late Cretaceous (78–100 Ma) in Bali (Hall & Spakman, 2015; Widiyantoro & van der Hilst, 1996). Plate motion models constructed from seafloor spreading rates, transform fault azimuths, and global positioning system measurements suggest a relatively high convergence rate between the Indo-Australian and Eurasian plates that increases from 5.5 cm/yr in Sumatra to 7.3 cm/yr near Timor (Bock et al., 2003; DeMets et al., 2010; Minster & Jordan, 1978) (Figure 1). The morphology and penetration depth of subducted lithosphere are well defined by the earthquake hypocenters that vary substantially along the strike of the plate boundaries. East of Java, the subducted oceanic lithosphere can be traced down to the base of the mantle transition zone (MTZ), whereas the seismicity is predominantly confined to the top 300 km beneath central and western Sumatra (Cardwell & Isacks, 1978; Hamilton, 1974). The subducting oceanic lithosphere is further evidenced by the presence of a high-velocity zone (Amaru, 2007; Fichtner et al., 2010; Fukao & Obayashi, 2013; Lekić & Romanowicz, 2011; Puspito et al., 1993; Widiyantoro & van der Hilst, 1996), which appears to penetrate into the lower mantle at a near-vertical angle beneath Java and Bali and potentially flattens at an approximate depth of 1,500 km (Puspito & Shimazaki, 1995; Replumaz et al., 2004; Widiyantoro & van der Hilst, 1997). In contrast, the slab beneath the Banda trench exhibits a shallower angle and its seismic signature can mainly be detected within and above, but not below, the MTZ (Spakman & Hall, 2010).

Characteristics of the MTZ seismic discontinuities offer additional constraints on the morphology and thermochemical effects of the Sunda slab. In an olivine-dominated upper mantle, the solid-solid phase transitions

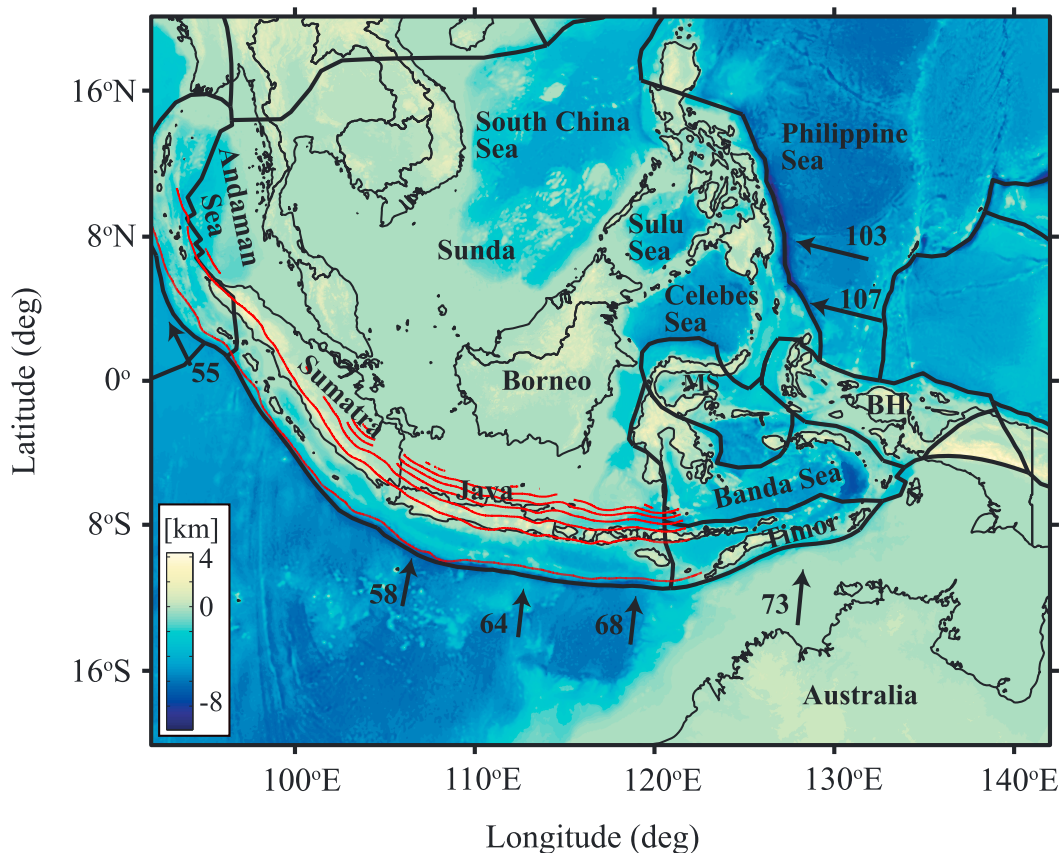


**Figure 1.** A topographic map of the study area. The black thick lines indicate the major plate boundaries after Bird (2003). The black arrows show the direction of plate motion with respect to the Sunda block, and their relative convergence rates are measured in cm/yr. The red lines denote the slab contours taken at a constant interval of 100 km (Hayes et al., 2012). Abbreviations: MS, Molucca Sea; BH, Birds Head.

from olivine to  $\beta$ -spinel and  $\gamma$ -spinel to perovskite+magnesiowustite mark the upper and lower boundaries of the MTZ at the nominal depths of 410 and 660 km, respectively (Anderson, 1967; Ito & Takahashi, 1989; Jeanloz & Thompson, 1983). Due to their opposite Clapeyron slopes, the thickness of MTZ is expected to increase in cold areas (e.g., subducting slabs) and decrease in warm regions (e.g., upwelling plumes) (Ito & Takahashi, 1989; Katsura & Ito, 1989). For this reason, the topography of the 410 km and 660 km seismic discontinuities (for short, the 410 and the 660) has been widely investigated through converted (Lawrence & Shearer, 2006; Saita et al., 2002) and reflected (Flanagan & Shearer, 1998; Gu et al., 2003; Houser et al., 2008) waves. Both types of observations indicate a local thickening of the MTZ along Java and southeastern Sumatra, ranging from 20 to 55 km and coinciding with a high-velocity anomaly within the MTZ (Fukao & Obayashi, 2013; Widijantoro & van der Hilst, 1996). Based on P-to-S converted waves (Saita et al., 2002), a narrow MTZ is found beneath northern Borneo and western Sulawesi, while the earlier observations from mantle reflections suggested that the thickness of the MTZ could increase by up to 20 km in the same region (Gu et al., 2003; Houser et al., 2008; Lawrence & Shearer, 2008).

Limited station distribution, lateral smoothing, and low data density remain major hurdles in the interrogation of the MTZ structure and dynamics in the Sunda arc subduction system. Conventional techniques such as delay-and-sum approaches have been used to image broad topographic variations on the discontinuities (Deuss, 2009; Gu et al., 1998, 2003; Shearer, 1993), though reliable detection of, and accurate resolution on, local-scale anomalies require more advanced algorithms and imaging philosophies (An et al., 2007; Cao et al., 2010; Dahlen, 2005; Schultz & Gu, 2013; Zhang et al., 2017; Zheng et al., 2015). In this study we investigate the topography of the 410 and 660 beneath SE Asia from prestack depth migration of SS precursor waveforms.

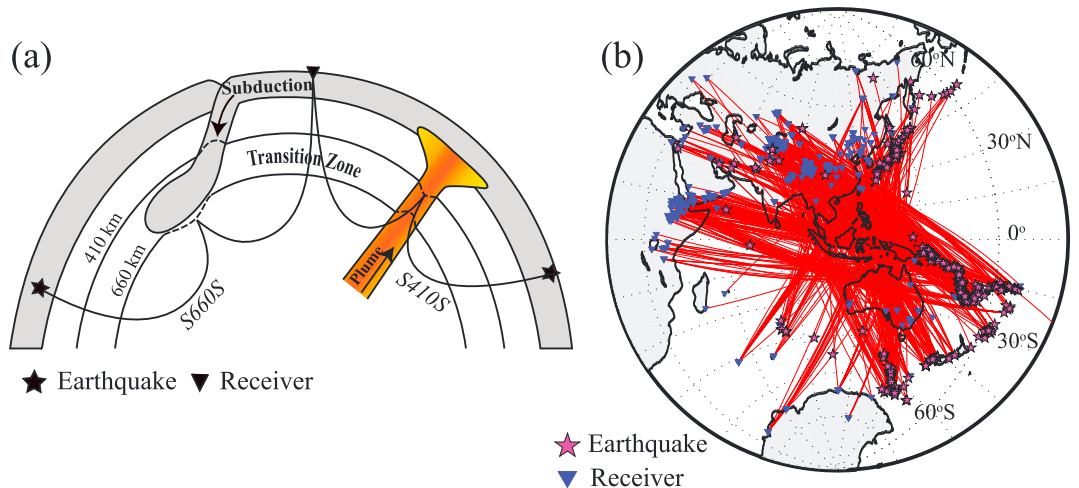


**Figure 2.** (a) The schematic diagram illustrates the SS precursor raypaths and the expected perturbations on the discontinuity depths in the presence of a cold subducting slab and a hot mantle plume in an isochemical mantle. (b) Distribution of the earthquake (stars) and seismic station (inverted triangles) locations used in this study. The line segments indicate the geometrical paths of SS precursors.

We demonstrate that the migration process using an array of precursors can effectively reduce the size of the Fresnel zone and enhance the resolution, which provides a critical window into the complex geometry and mantle temperature associated with the Sunda arc subduction.

## 2. Data and Method

### 2.1. Data Selection

Our main observational constraint is SS precursors, which are shear wave underside reflections off mantle interfaces near the midpoint between the earthquake and receiver (Flanagan & Shearer, 1998; Gu et al., 1998; Shearer, 1993) (Figure 2a). The precursors arrive before the main SS phase (i.e., surface reflection) due to their shorter propagation paths. We include broadband, long-period SH-polarized seismograms from  $M_w > 5.5$  earthquakes recorded between 1990 and 2015, with epicentral distances ranging from  $80^\circ$  to  $160^\circ$ . We restrict the reported earthquake depths to 75 km or less to avoid the potential interference from depths phases (e.g.,  $sSS$ ), while the selected distance range minimizes the interference from topside reflections (i.e.,  $S_{diff}$  postursors) and  $ScSScS$  precursors (Deuss, 2009; Schmerr & Garnero, 2006; Zheng et al., 2015). After removing the instrument responses, all transverse component seismograms are filtered between corner periods at 5 s and 50 s using a Butterworth band-pass filter. The waveforms of SS precursors are typically filtered at longer periods (e.g., above 15 s period), but shorter period filters can be effective at reducing the Fresnel zone size and increasing the resolution of mantle reflectivity when dense data coverage is available (Schmerr & Garnero, 2006). The filtered seismograms are subjected to a signal-to-noise ratio (defined as the ratio between the maximum amplitude of SS and that of noise in a precursory window; Gu et al., 2012) criterion, and only traces with signal-to-noise ratios greater than 3.0 are retained for the subsequent analysis. The final data set consists of 1,007 high quality, transverse component waveforms from 322 events (Figure 2b). The density of seismic stations is high in the Northern Hemisphere (nearly 90% of stations in China and eastern Africa), while the majority of earthquakes (~60% of events) occur in the southwestern Pacific and Tonga subduction zones.

### 2.2. Time-Domain Stacking Method

Due to the path similarity between the SS and its precursors (Schultz & Gu, 2013), the depths of reflectors can be effectively estimated from the differential times between the surface and mantle reflections. We deconvolve the SS waveforms, which share similar source effects with precursors, from the transverse component seismograms and normalize their maximum amplitudes to unity to equalize the source (Lessing et al., 2014; Shearer et al., 1999). The resulting waveforms are then time shifted to account for variations in crustal thickness, surface topography (CRUST2.0; Bassin (2000)) and mantle heterogeneity (S20RTS; Ritsema et al. (1999)) along the ray paths. The former two corrections assume that the surface structure does not show significant variations over the effective Fresnel zone of SS. To correct for moveout, we employ the local stretch zeroing (LSZ) method introduced by Kazemi and Siahkoohi (2012). This method eliminates stretching by dividing data

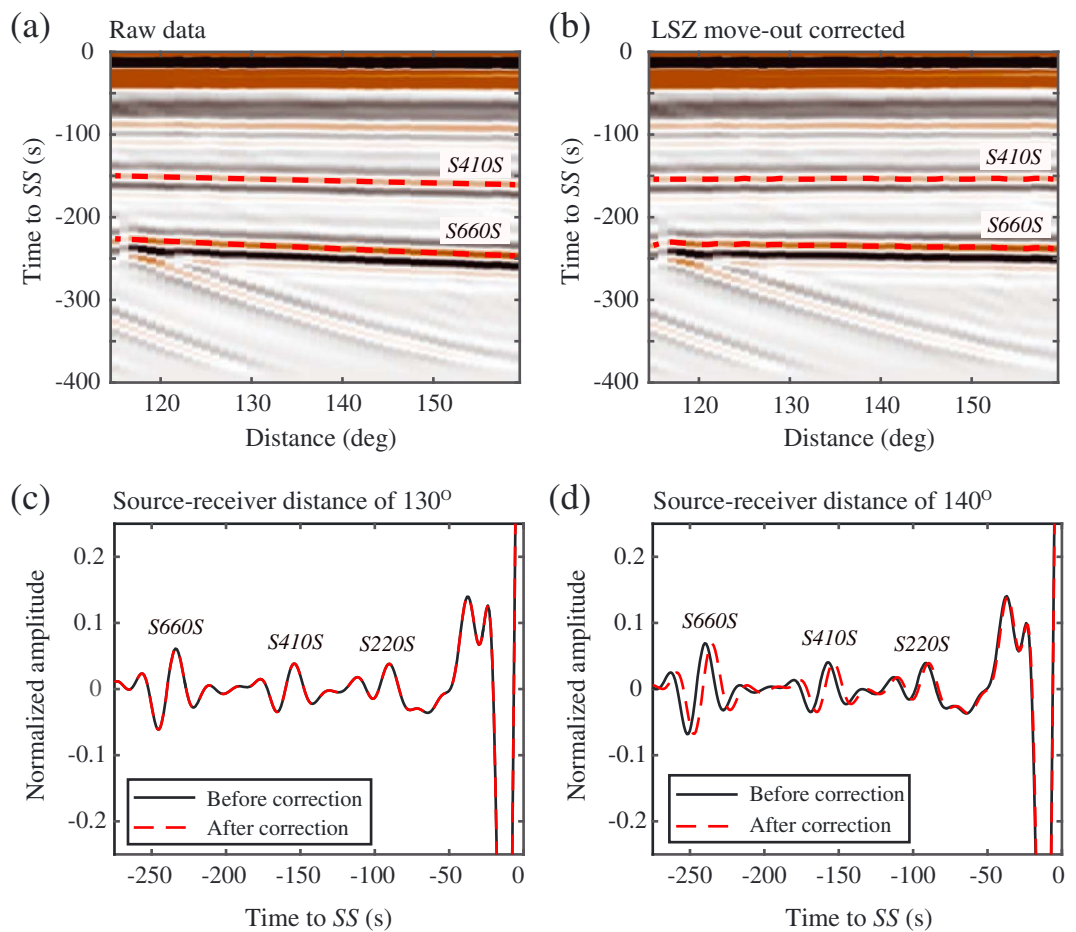


**Figure 3.** A synthetic test to demonstrate the effectiveness of the LSZ method for moveout correction. (a) A synthetic record section of SS precursors calculated based on PREM (Dziewonski & Anderson, 1981) before moveout correction. (b) Moveout-corrected data using the LSZ method. The red dashed lines indicate the S410S and S660S precursors. (c, d) A comparison between the precursor waveforms before (black solid lines) and after (red dashed lines) moveout correction for epicentral distances of 130° and 140°, respectively. The differential time shifts associated with the three major interfaces (i.e., the 220, 410, and 660) are accurately computed using the LSZ method.

into few time windows confined to the theoretical curves attributed to the reflection events (i.e., the mantle discontinuities). The effectiveness of the LSZ approach in moveout correction of SS precursors is investigated for synthetic waveforms calculated using PREM (Dziewonski & Anderson, 1981). Figure 3 shows the results of the LSZ method where the theoretical curves are calculated using the PREM-predicted arrival times of  $SdS$  (where  $d$  represents a discontinuity depth) and a reference source-receiver distance of 130°. This approach considers the differential moveouts among the precursory arrivals while avoiding distortions of pulse shapes (see Figures 3c and 3d).

### 2.3. Depth Migration

Migration is a key step in seismic data imaging, which spatially relocates the recorded signals to their true positions to improve the image quality and accuracy (Gazdag & Sguazzero, 1984; Gray et al., 2001; Sheriff & Geldart, 1995). The migration process is particularly effective in studies of tectonically complex regions (e.g., subduction zones and hotspots), where diffraction and scattering caused by small-scale variations in discontinuity depth can adversely affect the imaging resolution (Braña & Helffrich, 2004; Frederiksen & Revenaugh, 2004; Lessing et al., 2015; Neele et al., 1997; Rost & Thomas, 2009; Schultz & Gu, 2013; Thomas et al., 2004). Several depth migration algorithms have been utilized in exploration or global seismic applications, which include Kirchhoff (Etgen et al., 2009; Schneider, 1978), reverse time (Baysal et al., 1983; Biondi & Shan, 2002; Chang & McMechan, 1994), and wave-equation (Claerbout & Doherty, 1972; Gazdag, 1978; Kühl & Sacchi, 2003) migrations. In this study we adopt the Kirchhoff method for its simplicity and low computational cost.

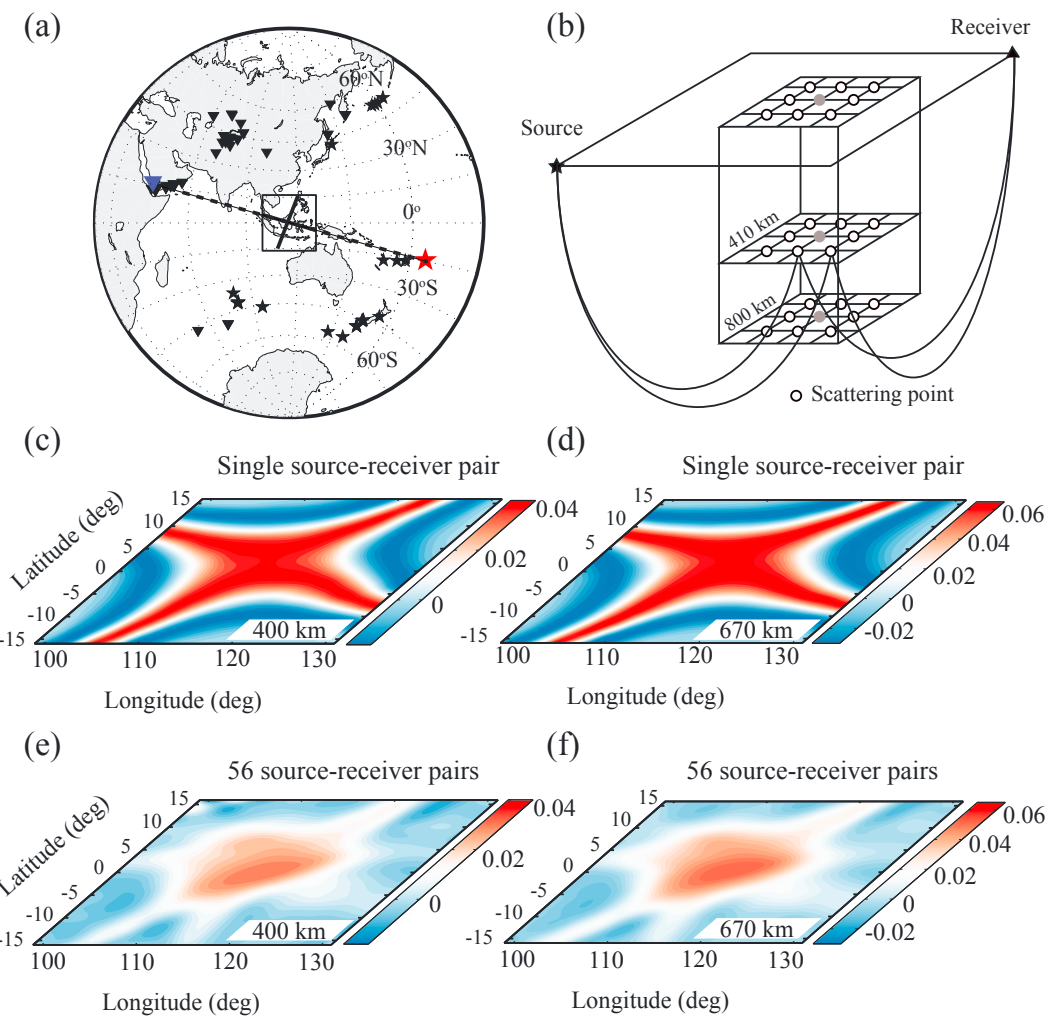


**Figure 4.** An array migration example showing the reflections at 400 and 670 km depths. (a) Distributions of the 56 source-receiver pairs that sample the area outlined by the black box. The stars and triangles represent the locations of the sources and receivers, respectively. (b) A schematic drawing of SS precursors reflected off the scattering points (open circles). The gray circles represent the reflection points halfway between the source and receiver. (c, d) Fresnel zones of SS reflections at the respective depths of 400 and 670 km for a given source-receiver pair (indicated by the red star and blue triangle in Figure 4a). (e, f) Same as Figures 4c and 4d but consider the contributions from all source-receiver pairs. The color bars indicate the stacked amplitude of the migrated energy.

Prestack (rather than poststack) migration is utilized to preserve the finer details contained in the SS precursor waveforms. Our algorithm searches for the energy arriving before SS, which is inundated by nonspecular reflections and point scatterers, and traces rays through 3-D models of the crust and mantle shear velocities.

To evaluate the effectiveness and accuracy of Kirchhoff depth migration, we introduce an array of sources and receivers sampling the area indicated in Figure 4a. Synthetic seismograms are then calculated based on the global shear velocity model S20RTS, assuming the theoretical reflections that occur at 220, 400, and 670 km depths below the center of the targeting area. We then adopt a grid of  $32^\circ$  by  $32^\circ$  with  $2^\circ$  lateral spacing (centered on  $0^\circ$  latitude and  $115^\circ$  longitude), and the depths range from 0 to 800 km at a constant increment of 2 km (see Figures 4a and 4b). Ignoring the finite frequency effect of precursors on discontinuity depths (Dahlen, 2005; Zhao & Chevrot, 2003), travel times of mantle reflections are subsequently calculated from each grid point (considered as a point scatterer) to each source as well as to each seismic station by tracing rays three-dimensionally through the same velocity model. Finally, the interpolated amplitude on each seismogram is assigned to the corresponding grid point and stacked (Rost & Thomas, 2009; Thomas & Billen, 2009). In theory, the diffracted energy should stack constructively at the location of the true reflection point.

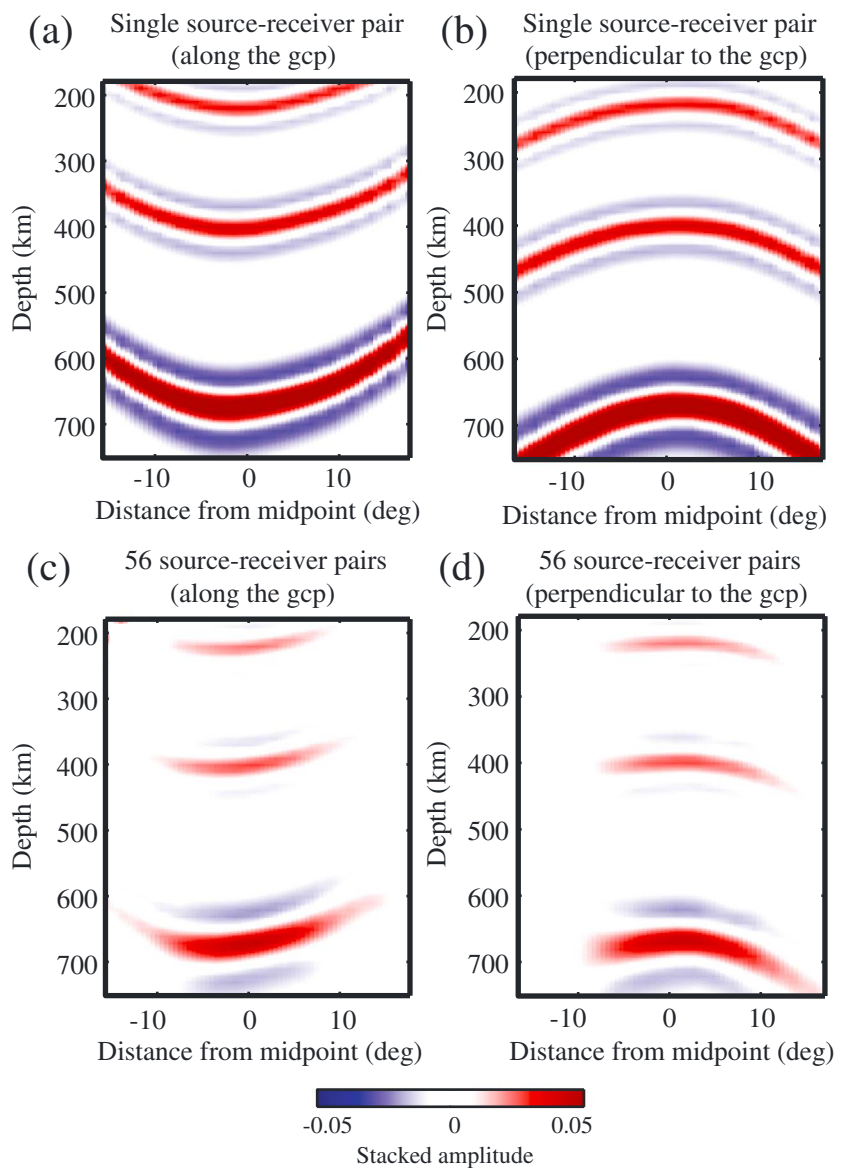


**Figure 5.** Array migration results using a single source-receiver pair (Figures 5a and 5b) and 56 source-receiver pairs (Figures 5c and 5d). (a, b) Vertical cross sections along and perpendicular to, respectively, the great circle path (gcp) connecting a given source-receiver pair indicated in Figure 4a. (c, d) Similar to Figures 5a and 5b but for all source-receiver pairs. The color bar indicates the stacked amplitude of the migrated energy.

The migration results for a single source and receiver pair at 400 and 670 km depths (Figures 4c and 4d) suggest that the maximum stacked amplitude is distributed along a minimax-shaped isochron (Gu & Dziewonski, 2002; Lawrence & Shearer, 2008; Rost & Thomas, 2009; Schmerr & Thomas, 2011; Shearer, 1993). In comparison with a single source-receiver pair scenario, the Fresnel zone becomes more regular using an array of precursor waveforms since contributions from multiple raypaths collapse the stacked energy to the true reflection point (Figures 4e and 4f). Based on the data density, this array migration process can reduce the effective Fresnel zone size to 500–700 km laterally.

Figure 5 shows two vertical cross sections through the center of the three-dimensional volume of migrated SS precursors. The minimax shape of the Fresnel zone is responsible for the concave up (see Figures 5a and 5c) and concave down (see Figures 5b and 5d) natures of the isochrons along and perpendicular to the great circle path, respectively (Gu et al., 1998; Neele et al., 1997; Shearer, 1993). This result implies that the along-(off-)axis scattering would map a hypothetical reflector to a shallower (deeper) depth with the same arrival time

(Shearer et al., 1999). By accounting for the contributions from the entire seismic array, the migration process reduces both the effective size of the Fresnel zone and the spreading of the migrated energy along the isochrons (Rost & Thomas, 2009) (see Figures 5c and 5d).

### 3. Results

Based on our resolution test using an array migration process, the data are grouped into equal-sized spherical caps of  $5^\circ$  radius, according to the theoretical reflection points of SS, to ensure sufficient resolution and sampling density (Figure 6). To obtain laterally coherent results, circular caps are sorted along 14 parallel profiles (with  $2^\circ$  cross-line spacing and an average of  $\sim 75\%$  overlap between two adjacent averaging caps) approximately perpendicular to the Java trench (see Figure 6). The grid, which consists of 490 imaging points, provides an average nominal lateral resolution of 500 km in the study region. The data coverage is particularly dense in the northwestern and southwestern ends of the study region, where a significant number of caps contain more than 100 reflections (see Table S1 in the supporting information). We examine the precursor waveforms in the time and depth domains independently to provide a cross-check on the accuracy of the recovered depth anomalies. First, the LSZ moveout-corrected data are gathered into common midpoint bins and stacked to obtain the amplitudes and travel times of precursory arrivals (sections 3.1 and 3.2). In the subsequent experiment, we derive independent estimates of depth distributions of the 410 and 660 using raw S<sub>d</sub>S waveforms without moveout and mantle heterogeneity corrections (section 3.3).

#### 3.1. SS Precursor Amplitude

Unlike conventional Kirchhoff migration approaches (Hanitzsch, 1997), our algorithm weights each seismogram equally to avoid complexity. Hence, the amplitude information is extracted from the time-corrected waveforms. After applying crustal and mantle heterogeneity corrections, we stack the waveforms using the LSZ moveout technique based on the differential times between the SS, S<sub>220S</sub>, S<sub>410S</sub>, and S<sub>660S</sub> phases (PREM; Dziewonski & Anderson, 1981) relative to a reference source-receiver distance of  $130^\circ$ . The amplitudes of S<sub>410S</sub> and S<sub>660S</sub>, extracted from the maxima within a 30 s window centered on the predicted times (PREM; Dziewonski & Anderson, 1981), reveal large-scale reflectivity structures at the MTZ discontinuities beneath SE Asia (Figures 7a and 7b). A NW-SE trending low-amplitude zone is observed near the 410 (see Figure 7a) along the Java trench, roughly parallel to the strike of the northward dipping Wadati-Benioff zone of deep-focus earthquakes (see Figure 6); the minimum amplitude of S<sub>410S</sub> reaches  $\sim 2\%$  of that of SS beneath western Java and the Timor trough. The measured reflectivity at the top of the MTZ does not vary significantly beneath Borneo and northern Sundaland, showing similar values to the regional average of 0.053. On the other hand, a strong S<sub>410S</sub> is observed east of the Philippine trench, below which the maximum amplitude is nearly twice the regional average.

The reflection amplitude of S<sub>660S</sub> shows markedly increased amplitudes along the Java trench relative to its regional average of 0.048 (see Figure 7b). East of Sumbawa, enhanced reflections continue northward and reach their maximum at approximately 0.1 beneath the Banda Sea. Similar to S<sub>410S</sub>, S<sub>660S</sub> exhibits low to moderate reflection amplitudes beneath the Borneo and Sunda plates (see Figure 7b).

Inherent noise and limited data coverage could cause significant uncertainties in the amplitude measurements. To assess the amplitude robustness and reliability, we introduce a bootstrap resampling procedure (Deuss, 2009; Dokht et al., 2016; Efron & Tibshirani, 1991) to estimate the standard errors by repeating the measurements using 200 randomly selected subsets of the data traces (Figures 7c and 7d). Based on the distribution of bootstrap measurements, we conclude that the major amplitude anomalies lie within the 95% confidence level and the estimated errors do not exceed 0.021 and 0.025 for S<sub>410S</sub> and S<sub>660S</sub>, respectively.

#### 3.2. SS Precursor Travel Time

Using the same stacked seismograms, we are able to determine the arrival times of SS precursors accurately (Figure 8). The S<sub>410S</sub> times (see Figure 8a) indicate early arrivals with respect to SS in the vicinity of the Wadati-Benioff zone beneath western Java and the entire Banda Sea,  $\sim 8$ – $10$  s earlier than the regional average of  $-156.4$  s. Most notably, the S<sub>660S</sub> times in the eastern part of the study area are 8–15 s shorter than the regional average of  $-229.25$  s, extending from the Indian ocean side of the Flores Island northward toward the Molucca Sea. Both S<sub>410S</sub> and S<sub>660S</sub> are, however, delayed beneath Borneo and the western Sulawesi regions (see Figures 8a and 8b).

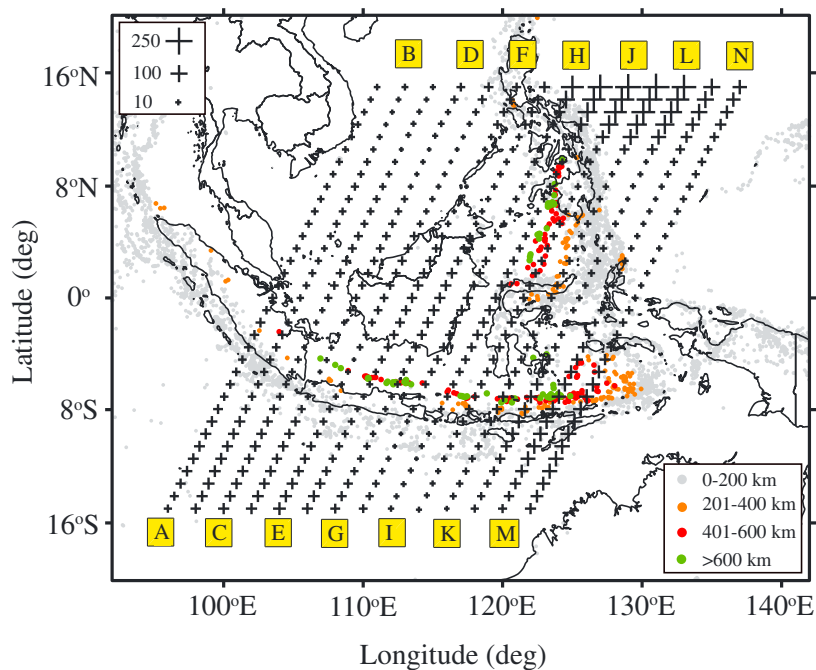


**Figure 6.** A map of the study area showing the locations of the imaging points (black crosses), which are sorted along 14 parallel profiles (A-N) oriented approximately perpendicular to the arc. The sizes of crosses correspond to the total number of contributing traces of each point. The colored circles indicate the deep focal earthquakes that are grouped into the four different depth intervals (0–200 km: gray circles; 201–400 km: orange circles; 401–600 km: red circles; >600 km: green circles).

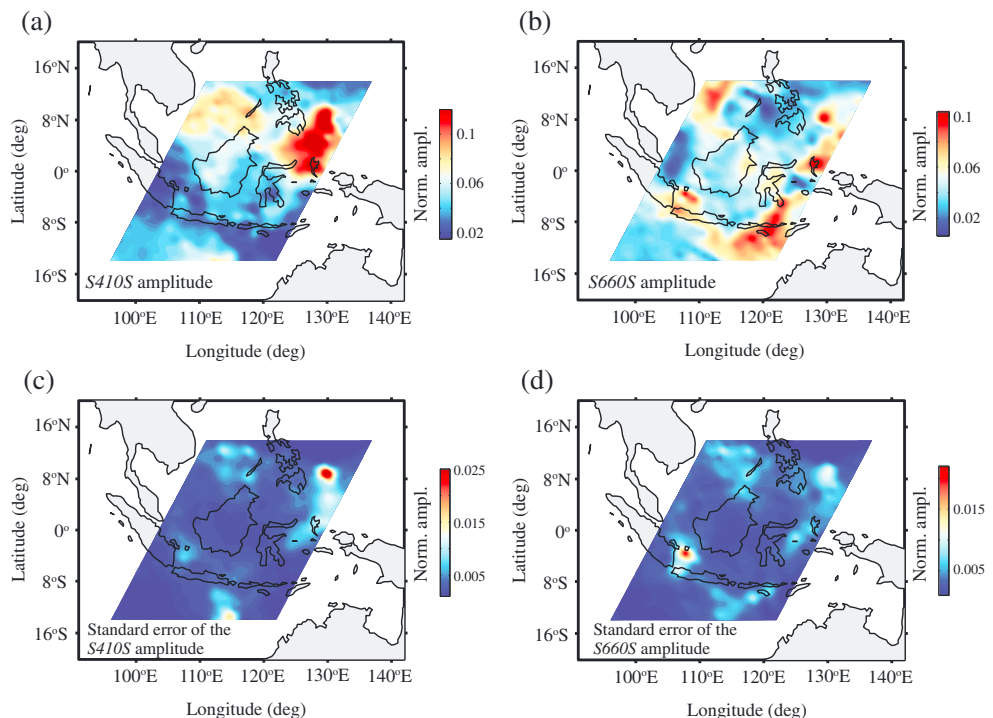


**Figure 7.** Interpolated reflection amplitudes of the (a) S410S and (b) S660S. The precursor amplitudes are normalized to that of SS. (c, d) The standard errors of the reflection amplitudes based on a bootstrapping analysis. The red and blue colors indicate the high- and low-amplitude precursory arrivals, respectively.

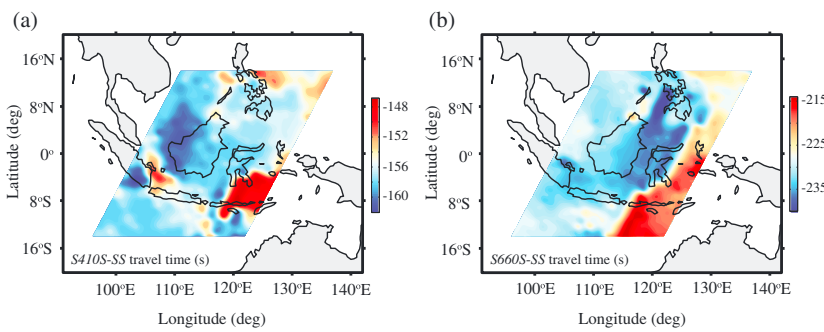


**Figure 8.** Interpolated differential times of (a) S410S-SS and (b) S660S-SS. The red and blue colors represent early and delayed SS precursor arrivals, respectively.

To assess the effect of time corrections, which can introduce unwanted variations in both the amplitude and timing of the secondary reflections, we repeated the time domain stacking procedure using a different shear velocity model (i.e., TX2007; Simmons et al., 2007) and found no apparent changes in reflectivity. In other words, a reasonably accurate model of the mantle structure should produce reliable reflections from the major discontinuities.

### 3.3. MTZ Discontinuity Depth

The topography of MTZ discontinuities can be constructed from the depth-migrated volume of the SS precursor data set (Figure 9). For reliable results we independently migrate the precursor waveforms using S-wave

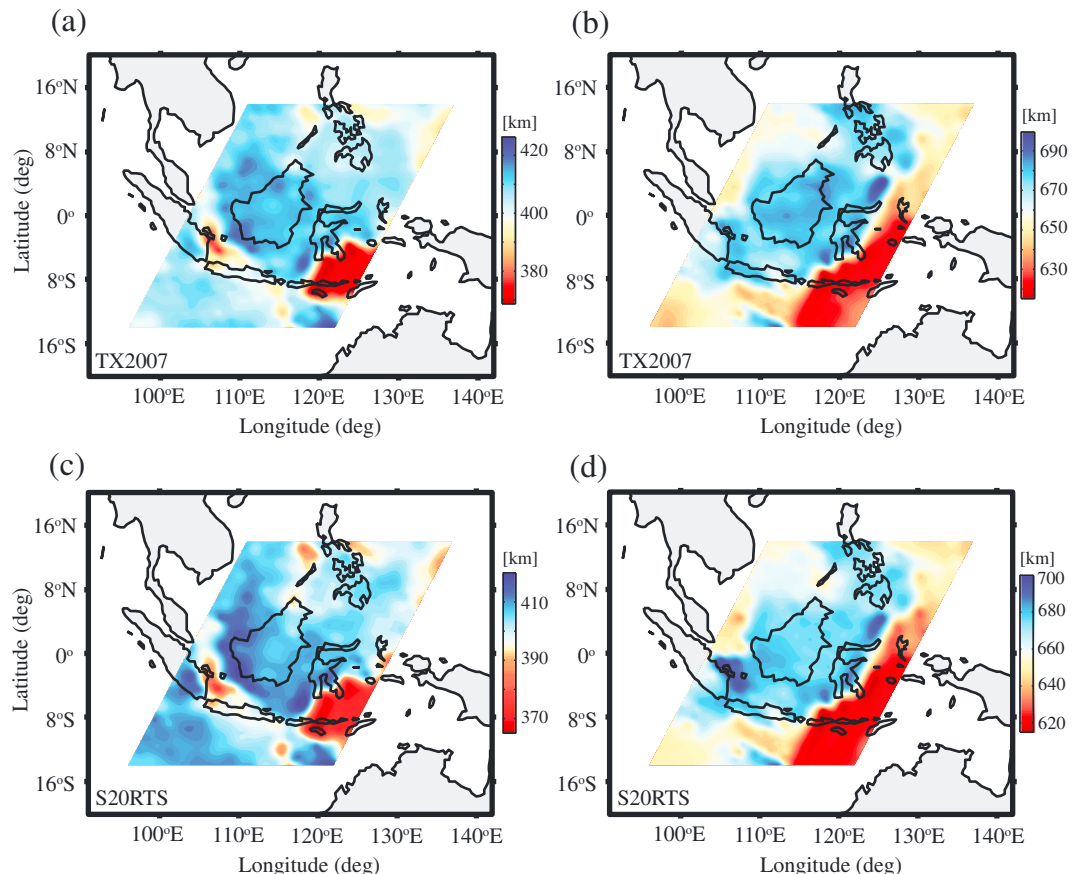


**Figure 9.** (a, b) Topographies of the 410 and 660, respectively, calculated from the depth migration of SS precursors using the S-wave model of TX2007 (Simmons et al., 2007). (c, d) Similar to Figures 9a and 9b, but using the S-wave model S20RTS (Ritsema et al., 1999). The red and blue colors indicate elevation and depression, respectively.

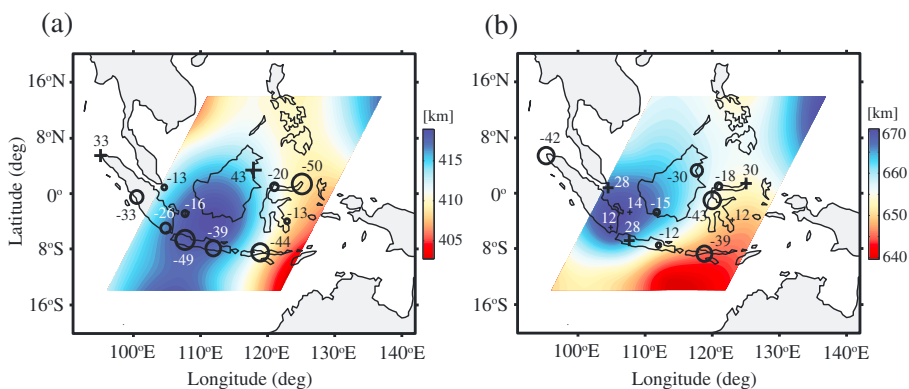


**Figure 10.** Discontinuity topography. The color contours show the (a) 410 and (b) 660 topography from Gu et al. (2003). The red and blue colors show the discontinuity elevation and depression, respectively. The open circles and crosses denote the elevation and depression, respectively, of the MTZ discontinuities from Saita et al. (2002). The depth anomalies from Saita et al. (2002) are plotted relative to the corresponding global averages of 418 km and 660 km for the 410 and 660 (Flanagan & Shearer, 1998).

models of TX2007 (Figures 9a and 9b) and S20RTS (Figures 9c and 9d). The results based on these two different velocity models are generally consistent, despite slightly deeper (1.2–3 km) discontinuity depths from TX2007 (see Figure 9). The calculated regional averages for the 410 and 660 are 403 km and 662 km, respectively, comparable to their corresponding global averages of 410–420 km and 650–660 km (Flanagan & Shearer, 1998; Gu et al., 2003). The 410 is elevated beneath eastern Sumatra and western Java, the Flores Sea, and Banda Sea by up to 29, 35, and 37 km (see Figures 9a and 9c), respectively. In eastern Sumatra and western Java, the topography of the 410 is strongly anticorrelated with that of the 660, which is depressed by 20–40 km with respect to its regional mean (see Figures 9b and 9d). On the other hand, the depth of the 410 beneath the Banda Sea and Flores Island positively correlates with that of the 660, showing 40–45 km elevation in this area. Both discontinuities are depressed beneath Borneo, western Sulawesi, and the Celebes Sea, although the undulations on the 410 (+5 to +10 km) are significantly less than those on the 660 (+10 to +35 km).

Our measured MTZ discontinuity depths are generally consistent with those of Saita et al. (2002) from receiver function migration and Gu et al. (2003) based on joint inversion of the MTZ velocity and discontinuity topography (Figure 10). Despite differences in absolute depths, all three studies clearly identify elevated 410 and 660 beneath the eastern part of the study area. The lone exceptions are Sumatra and Java, where the underlying 410 is elevated by up to 50 km in the two regional studies but appears to be average in the former global analysis (Gu et al., 2003) (see Figures 9 and 10). We attribute this discrepancy to the different data densities and lateral resolutions.

The transition zone thickness beneath eastern Sumatra and western Java exceeds the global average of 241–242 km (Flanagan & Shearer, 1998; Gu et al., 1998; Lawrence & Shearer, 2006) by as much as 60 km (Figures 11a and 11b). These observations are comparable to the earlier reported values by Saita et al. (2002) and Gu et al. (2003), although the increase in MTZ thickness is less significant in the later study (approximately 15 km thicker than the global average; see Figure 11c). The MTZ beneath the Banda Sea shows only minor thickness variations but becomes 20–30 km narrower toward the north (the Molucca Sea) and south (the Australian side of the Timor trough) due to the substantial elevations of the 660 (see Figures 9 and 11). The most noteworthy difference among these studies is the MTZ beneath northern Borneo and western Sulawesi, where the present study shows a thick MTZ (270–275 km), while it was found to be narrower (approximately 200 km) in the earlier study by Saita et al. (2002) (see Figure 11).

Uncertainties in discontinuity depths are evaluated through recovery tests. To do so, we first calculate synthetic seismograms for the combination of sources and receivers that sample the area in westernmost Java (profile A in Figure 6) using shear velocities from S20RTS and the 410 and 660 depths from Gu et al. (2003). We add 3% Gaussian noise to the resulting synthetic seismograms according to the observed standard errors from bootstrap resampling of the real data (see Figure 7). To estimate the error due to the use of inaccurate model velocities in the migration process of precursors, we compare the heterogeneity corrections calculated

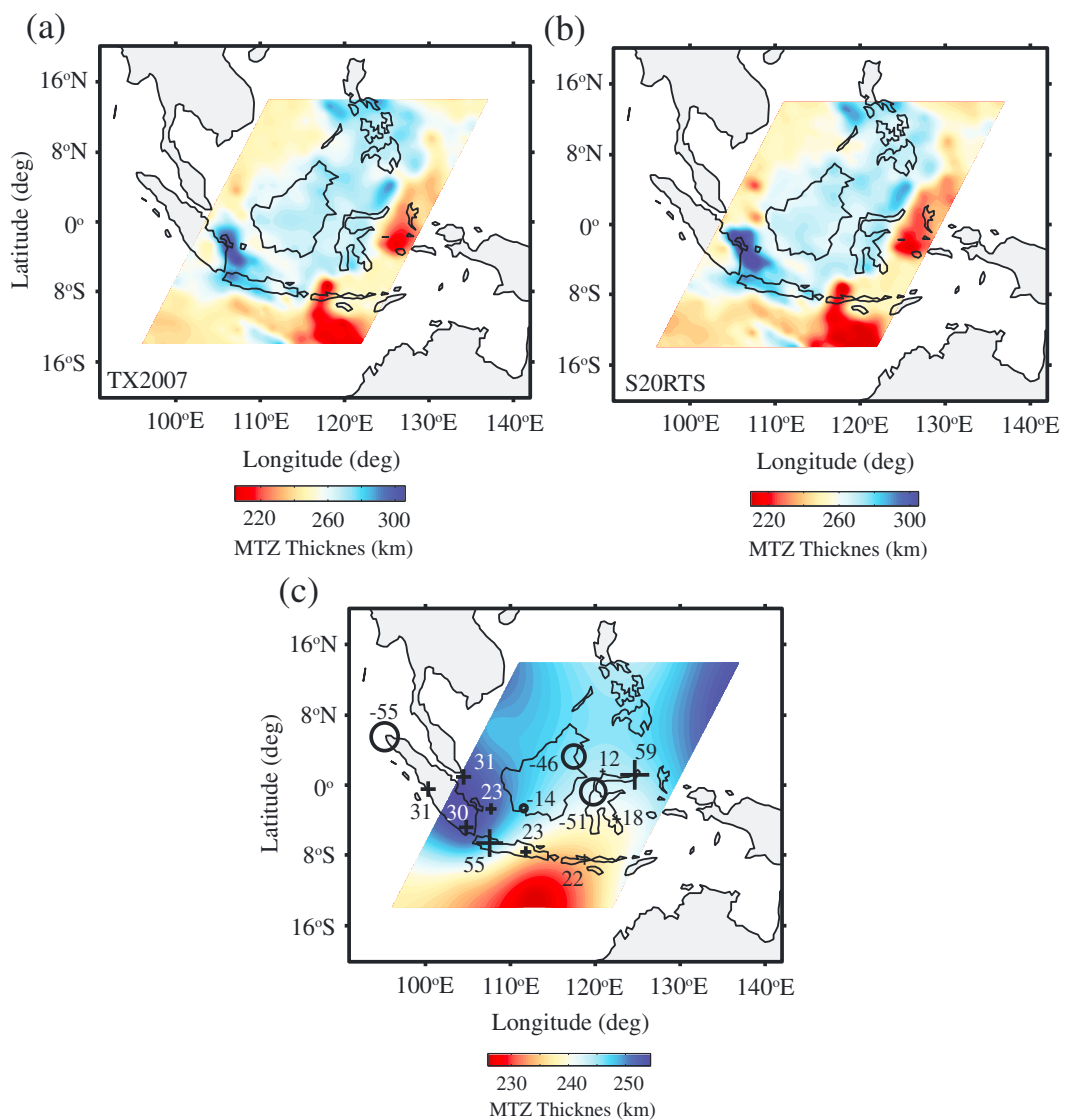


**Figure 11.** (a) MTZ thickness variations calculated from the migrated depths of the 410 and 660 km discontinuities using TX2007 (Simmons et al., 2007). (b) Similar to Figure 11a but using S20RTS (Ritsema et al., 1999). (c) The color contours represent the MTZ thickness measurements from Gu et al. (2003). The open circles and crosses show thinner and thicker transition zone regions, respectively, from Saita et al. (2002) relative to the global average of 241 km (Flanagan & Shearer, 1998).

from three different models: S20RTS, TX2007, and SEMum (Lekić & Romanowicz, 2011). The average difference between the resulting model correction is  $\sim 1.2$  s, with a standard deviation of  $\sim 0.9$  s (see Figures S1 and S2 in the supporting information). We then apply random time shifts within the interval  $(-3.0$  s,  $+3.0$  s), which corresponds to the upper limit of the 95% confidence interval of the estimated error in mantle correction, to the precursor waveforms. The resulting reflectivity image through the same migration procedure shows coherent reflections associated with the 410 and 660 (Figure 12a). The maximum absolute errors between the input and recovered depths of the 410 and 660 are  $\sim 4$  km and  $\sim 6$  km, respectively (see Figures 12b–12e), consistent with the previously reported error of  $\sim 5$  km for the 660 by Zhao and Chevrot (2003). A comparison between the migration results using S20RTS and TX2007 (presented in Figures 9a–9d) and those of using the more recent S-wave model SEMum also indicates a maximum difference of nearly 8 km for major depth anomalies among these models (Figure S3). The outcome of these investigations implies that the observed depth anomalies of up to  $\sim 35$  km (for the 410) and  $\sim 40$  km (for the 660) are unlikely to be artifacts associated with inaccurate seismic velocities.

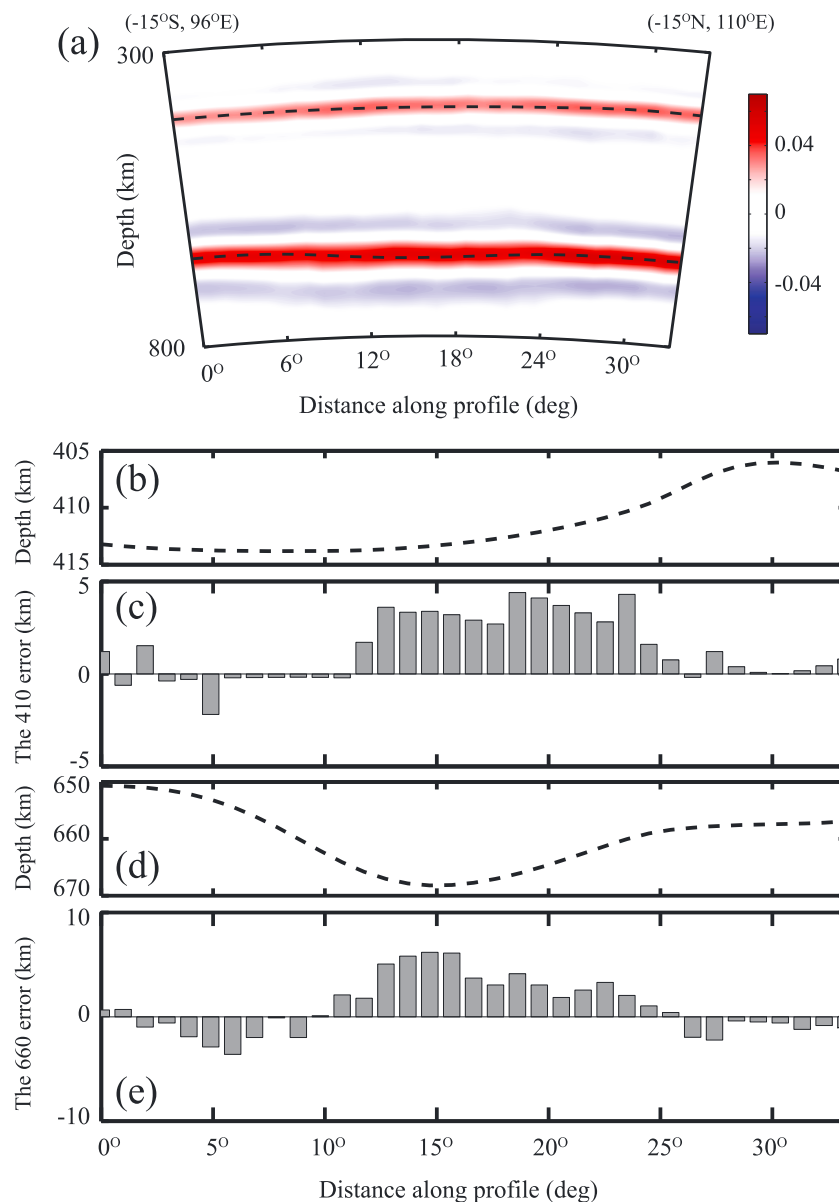


**Figure 12.** A synthetic recovery test for the depths of MTZ discontinuities along profile A of Figure 6. (a) A reflectivity cross section from the migration of synthetic SS precursors. The dashed lines indicate the input depths of the 410 and 660 from Gu et al. (2003). (b, e) Input depths of the 410 and 660, respectively. (c, e) Corresponding estimated errors in the recovered depths of the 410 and 660.

#### 4. Discussion

The mantle structure beneath SE Asia has been previously investigated using body wave travel time (Fukao & Obayashi, 2013; Fukao et al., 1992; Gorbatov & Kennett, 2003; Widjiantoro & van der Hilst, 1997) and waveform (Fichtner et al., 2010; Lekić & Romanowicz, 2011) tomography. The most prominent feature in the upper mantle in this region is a narrow, northward dipping high-velocity structure, which extends from the Sunda arc (in the west) to the Banda arc (in the east) (Figures 13a and 13b) and has been commonly attributed to the subducted Indo-Australian oceanic lithosphere underneath the Eurasian plate. Both  $P$  and  $S$ -wave data generally suggest a 1–2% increase in the seismic velocities within the MTZ beneath Sumatra, Java, the Flores, and Banda Seas (Amaru, 2007; Replumaz et al., 2004; Widjiantoro & van der Hilst, 1996) along the Wadati-Benioff zone of the descending slab (Cardwell & Isacks, 1978; Hamilton, 1974; Hayes et al., 2012). The detailed morphology

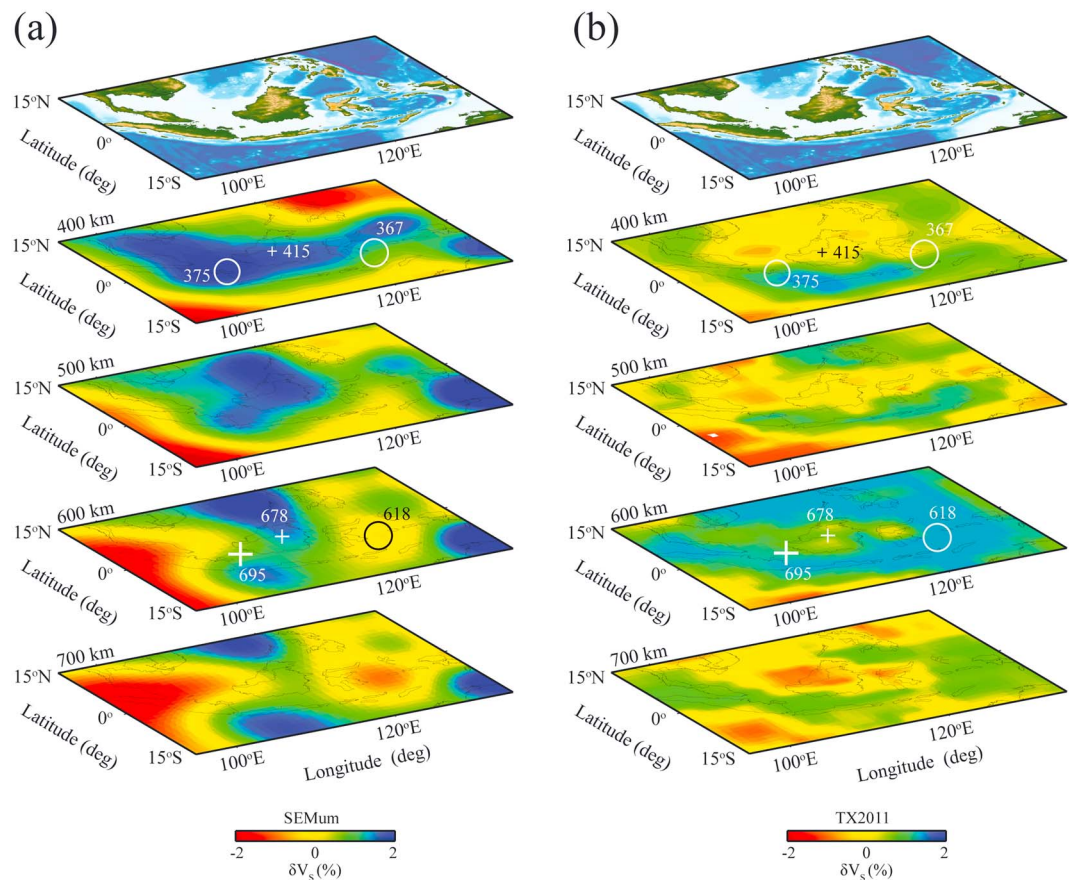


**Figure 13.** S-wave velocity perturbations from (a) SEMum (Lekić & Romanowicz, 2011) and (b) TX2011 (Grand, 2002) at 400 km, 500 km, 600 km, and 700 km depths (IRIS, DMC, 2013). The open circles and crosses indicate the major depth anomalies of the 410 and 660 from this study. The blue and red colors denote fast and slow seismic anomalies, respectively.

of subducting slab exhibits major lateral variations and different penetration depths along its strike (Hall & Spakman, 2015), which can locally affect the topographies of MTZ discontinuities.

Despite extensive global studies of *P* and *S*-waves (Andrews & Deuss, 2008; Deuss, 2009; Flanagan & Shearer, 1998; Gu et al., 2003; Lawrence & Shearer, 2006), variations in MTZ discontinuity depths beneath the SE Asia subduction zones have been thinly explored on the regional scale (Saita et al., 2002). In comparison with earlier analyses based on SS precursors (Deuss, 2009; Gu et al., 2003; Houser et al., 2008; Lawrence & Shearer, 2008), the current study takes advantage of vastly improved data coverage (due to a longer period of recordings) and enhanced resolution by considering scattering from the finer-scale depth perturbations of the discontinuities (Rost & Thomas, 2009). The resulting migrated SS precursor waveforms provide new constraints on the MTZ structure and the dynamical process therein that are associated with the subducting lithospheric plates beneath SE Asia.

#### 4.1. Java Subduction and Slab Gap

Our study reveals significant lateral variations in MTZ discontinuity depth and thickness along the Sunda arc (see Figures 9 and 11). The thickest part of the MTZ is observed under southwestern Sumatra and eastern Java (approximately 300 km on average), magnified by the contrasting topography of the 410 and 660 in response to the temperature effect of a sinking slab within the MTZ. According to a recent analysis by Fukao and Obayashi (2013), the *P*-wave velocities increase by 1.5% under the southeastern part of the Sunda arc (Figures 14a and 14b). This anomaly appears to extend into the MTZ at a steep angle, eventually terminating at approximately 1,500 km depth in the shallow lower mantle (Puspito & Shimazaki, 1995; Widijantoro & van der Hilst, 1997). Assuming an isochemical model, a 20 km topographic variation on the 410 or 660 would require

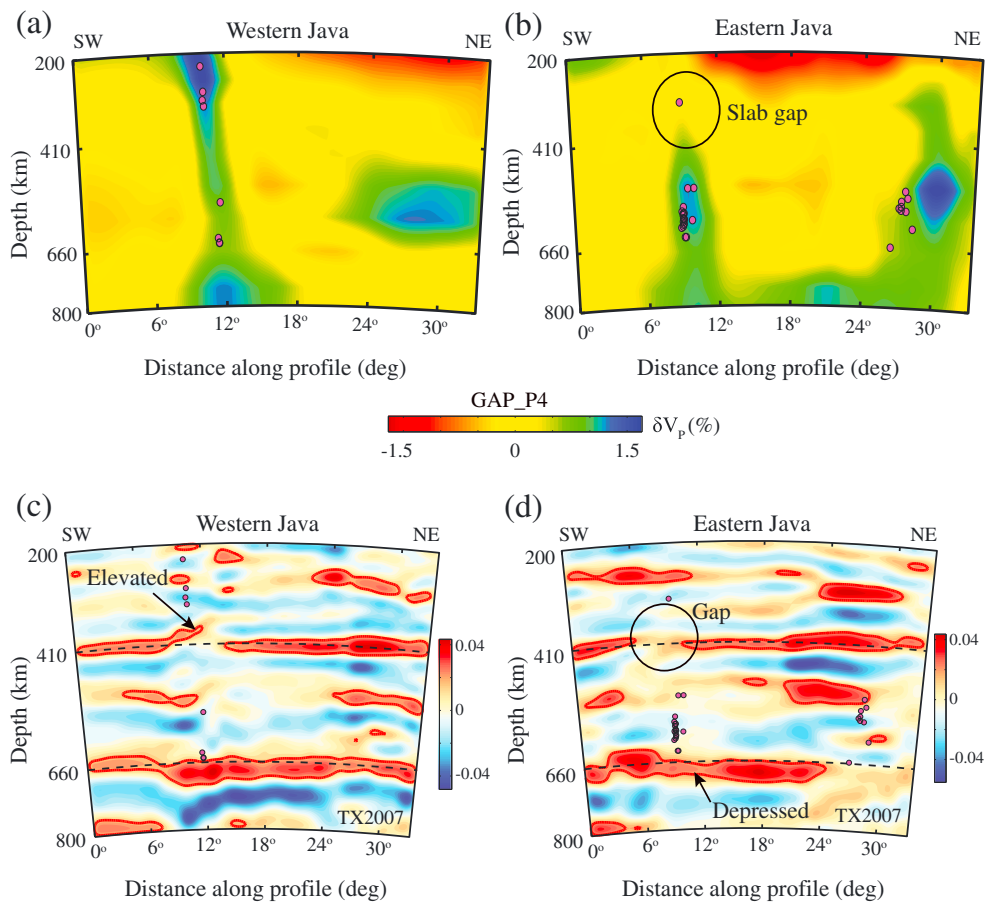


**Figure 14.** Vertical cross sections of variations in  $P$ -wave velocities beneath (a) western (along profile D of Figure 6) and (b) eastern (along profile H of Figure 6) Java from Fukao and Obayashi (2013). (c) Reflectivity cross sections of the migrated SS precursors beneath western Java using TX2007 (Simmons et al., 2007). (d) Similar to Figure 14c but beneath eastern Java. The magenta circles indicate the locations of deep earthquakes. The dashed lines indicate 410 and 660 km depths.

a temperature reduction of  $\sim 250$  K within the slab (Akaogi et al., 1989; Saita et al., 2002; Weidner & Wang, 1998). The 410 and 660 depths are highly correlated with the northward dipping high-velocity subducting lithosphere, where the 660 is locally depressed (by  $>20$  km) at the bottoming part of the slab (from  $8^\circ$  to  $14^\circ$  in Figures 14a and 14c). The 660 depression becomes less significant at larger distances from the bottoming section (670 km depth at  $24^\circ$  in Figure 14c), though the  $P$ -wave velocities show no evidence of slab stagnation within the MTZ. Further east, fast seismic velocities are well resolved near 660 km depth (see Figure 14d). Minor discrepancies could be explained by different spatial resolutions and averaging operators between the two studies.

Our measurements in western Java are consistent with these earlier findings. However, the depth of the 410 gradually increases toward the east and becomes nearly flat (with less than 5 km elevation compared to its regional average) beneath eastern Java (see Figures 14c and 14d), where average to weakly positive velocities have been previously documented at 300–500 km depths (Amaru, 2007; Fukao & Obayashi, 2013; Huang et al., 2015; Widjiantoro & van der Hilst, 1996, 1997) (see Figure 14b). The apparent absence of the subducting slab in the vicinity of the 410 beneath eastern Java coincides with a pronounced seismically quiescent zone along the trench at comparable depths (Puspito & Shimazaki, 1995; Widjiantoro & van der Hilst, 1996). This observation has led to the hypothesis of a “gap” or “tear” at the top of the slab (Hall & Spakman, 2015).

Different processes have been proposed as possible mechanisms for developing a tear in the slab, which potentially involve (1) local heterogeneity within the subducting lithospheric plate (Hall & Spakman, 2015)

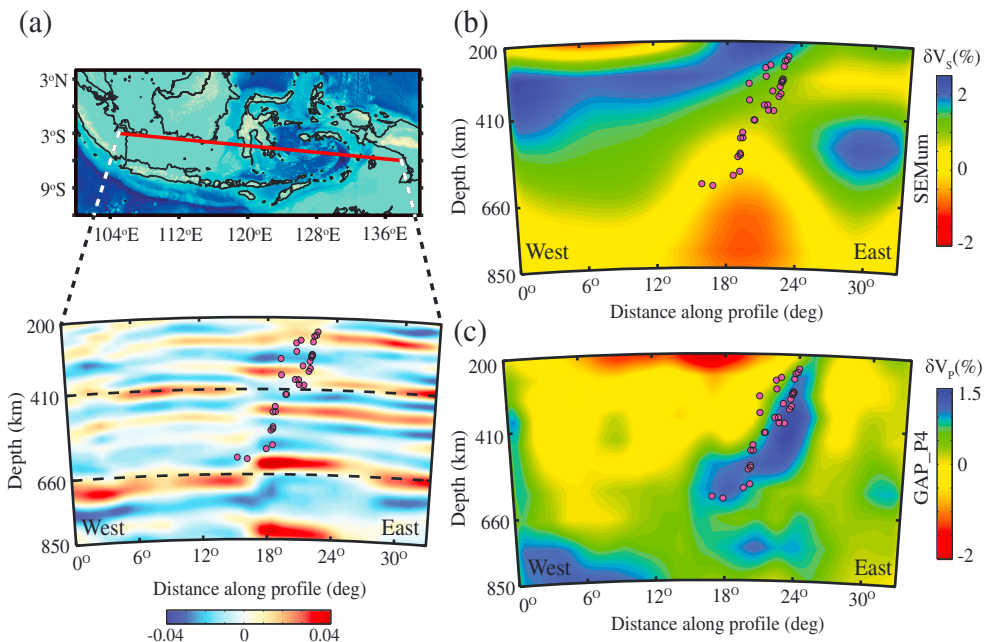


**Figure 15.** (a) A reflectivity cross section of the migrated SS precursors along W-E direction using SEMum (Lekić & Romanowicz, 2011). The red and blue colors represent high and low reflection amplitudes, respectively. The black dashed lines are drawn at 410 and 660 km depths. (b, c) Vertical cross sections of S and P-wave velocity perturbations, respectively, along the profile indicated in Figure 15a. The magenta circles indicate the locations of deep-focus earthquakes.

and (2) necking and thinning of the slab in the upper mantle (Widiyantoro & van der Hilst, 1996). Hall and Spakman (2015) suggest that a hole has been formed in the sinking slab after a buoyant oceanic plateau reached the Java trench at approximately 8 Ma, which was unable to subduct due to a lower density than the ambient lithosphere (Niu, 2014). In this scenario, the oceanic plateau collision blocks subduction and causes the trench to step backward relative to the incoming plate. Over time, the subduction of the oceanic lithosphere will resume behind the plateau and generate a vertical tear (hole) in the downgoing slab (Hall et al., 2009; Widiyantoro et al., 2011a). This hypothesis is supported by the discovery of potassium-rich magmatism, which has been linked to reduced fluid flux from the slab into the mantle wedge after the slab window passed beneath the arc in eastern Java (Edwards et al., 1994; Hall & Spakman, 2015). It is worth noting that smaller-sized gaps and tears have also been reported further east in the subducting slab beneath the Timor and Flores Islands (Hall & Spakman, 2015; Widiyantoro et al., 2011a); however, these features remain below the detection threshold of SS precursors from this study.

#### 4.2. MTZ Beneath the Banda Trench

The most notable depth anomalies are observed beneath the Banda Sea and its surrounding areas, where a narrow MTZ is detected (see Figure 11) due to a substantially elevated 660 (by nearly 40 km; Figure 9). An uplifted 410 likely results from the Miocene subduction of the Jurassic oceanic lithosphere at the Banda trench (Fichtner et al., 2010; Spakman & Hall, 2010), which deflects and becomes stagnant atop the MTZ (Widiyantoro et al., 2011b). The complex geometry of the slab is supported by a spoon-shaped high P-wave velocity zone in the asthenosphere beneath the Banda Sea and western Sulawesi (Amaru, 2007; Fukao & Obayashi, 2013; Lekić & Romanowicz, 2011; Widiyantoro et al., 2011a) (Figure 15), though its geometry is not well resolved in the S-wave model SEMum due to reduced spatial resolution (100 km vertically and 2° laterally) at greater depths (Figure 15b). While the MTZ phase boundaries (i.e., the 410 and 660) are expected to be anticorrelated, especially in the vicinity of the subduction zones (Gossler & Kind, 1996; Gu et al., 2003; Li & Yuan, 2003), the excess elevation of the 660 in this region requires the consideration of nonvertical dip of the subducting slab (Dokht et al., 2016; Gu et al., 2012). A vertical section of the migrated reflectivity along the west-east direction shows the negative correlation between the 410 and 660 depths along the Wadati-Benioff zone (Figure 15a), where the 660 reaches the maximum depth of 680 km directly beneath southeast Sulawesi. The observed 20 km depression of the 660 is consistent with the response of the postspinel phase transition from ringwoodite

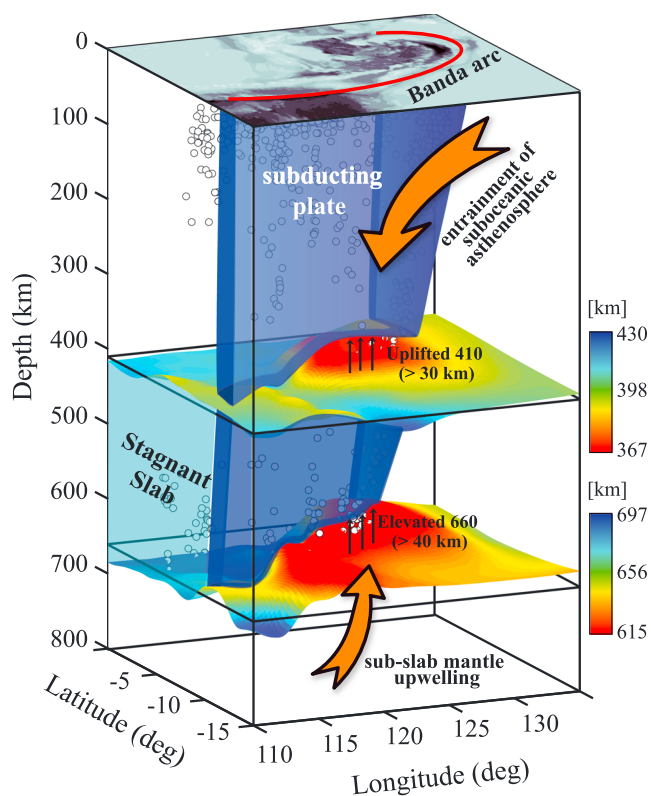


**Figure 16.** A schematic drawing of the subduction along the Banda arc. The presence of a low-velocity zone within the MTZ beneath the slab can be explained by the (1) entrainment of hot asthenospheric materials and (2) subslab mantle upwelling. The topographies of the 410 and 660 beneath the Banda trench are color coded and plotted at their respective depths. The white circles indicate the locations of deep-focus earthquakes.

excess temperature of 200 K beneath the downgoing plate at MTZ depths (Fukao & Obayashi, 2013; Honda et al., 2007; Morishige et al., 2010; Obayashi et al., 2006; Wang & Chen, 2009; Yu et al., 2017; Zhao et al., 2007). The thermal origin of low-velocity zone beneath the Pacific slab has been linked to the remnant of superplume heads (Honda et al., 2007) or hot mantle upwelling close to the sinking oceanic lithosphere (Obayashi et al., 2006; Wang & Chen, 2009) (Figure 16). These mechanisms could have direct implications for our observations, though the location of the observed thermal anomaly (southeastern edge of the study area) and its spatial extent remain somewhat enigmatic.

## 5. Conclusions

This study examines the depth and amplitude of the MTZ seismic discontinuities near the Sunda-Banda arc using SS precursors. Through migration imaging, we observe small-scale depth variations on the 410 and 660 across the SE Asia subduction zones. Beneath eastern Sumatra and western Java, a strong negative correlation between the 410 (elevated) and 660 (depressed) depths suggests significantly reduced temperature within the steeply dipping Indo-Australian slab. A flat 410 beneath eastern Java coincides with the absence of deep-focus earthquakes over the depth interval from 300 km to 500 km. These observations may be associated with the arrival of a buoyant plateau in the trench in the Late Miocene, which formed a vertical tear in the subducting slab.

Beneath the Banda Sea, enhanced amplitude of the 660 and 40 km elevation are evidence of low seismic velocities within the MTZ due to an increase in its temperature. The low-velocity anomaly above the 660 can be associated with (1) hot asthenosphere abducted by the downgoing slab and (2) subslab mantle upwelling. The results presented in this study provide a more detailed image of the mantle reflectivity structure beneath SE Asia, which can be strongly affected by the dynamics of the subducting slab.

to perovskite and magnesiowustite with a negative Clapeyron slope of approximately  $-2.8$  to  $-3.0$  MPa/K (Ito & Takahashi, 1989; Weidner & Wang, 1998) to a temperature decrease of  $>200$  K at the bottoming part of the slab (see Figure 15c).

Beneath the Banda Sea in eastern Indonesia, an elevated 660 is accompanied by high-amplitude S660S arrivals in the time domain stacks of precursor waveforms (see Figure 7b). These observations consistently suggest an increase in impedance contrast across a relatively shallow 660 due to the presence of a high-temperature anomaly at the base of MTZ. A 36 km elevation of the 660 (which is supported by a 40 km uplifted 660 beneath the Flores Sea from receiver function observations by Saita et al., 2002) requires a temperature increase  $>400$  K (Ito & Takahashi, 1989), assuming that the compositional effects can be neglected compared to thermal effects in the upper mantle (Piazzoni et al., 2007). This will result in a shear wave velocity reduction of approximately 3% (Stixrude & Lithgow-Bertelloni, 2005; Houser & Williams, 2010), which has rarely been documented by seismic tomography at depths greater than 600 km (see Figure 13 and the low-velocity anomaly in Figure 15b), partly due to poor ray coverage at greater depths and limited vertical resolutions (Bijwaard et al., 1998; Tajima & Grand, 1995) and different dependencies of P- and S-wave velocities on temperature (Widiyantoro et al., 2011a).

Different mechanisms have been proposed for the presence of subslab low-velocity zone. Entrainment of a thin layer of hot asthenospheric materials may have been possible due to (1) a nearby mantle plume (Phipps Morgan et al., 2007) and (2) shear heating in the suboceanic asthenosphere induced by the relative motion of overlying oceanic plate (Long & Silver, 2008). While the magnitude and size of the entrained high-temperature anomaly remain unclear and cannot fully explain the existence of a broad elevated 660, several recent studies, especially on the western Pacific subduction zones, have identified extensive low-velocity anomalies with an

In short, improving the resolution of mantle imaging can provide critical insights into the complex morphology, temperature, and dynamic process beneath the Java-Banda Sea region.

### Acknowledgments

We would like to thank Yunfeng Chen and Nasser Kazemi for their help during the preparation of this manuscript. We would also like to thank two anonymous reviewers and the Associate Editor, Sébastien Chevrot, for their constructive reviews. The facilities of IRIS Data Services, and specifically the IRIS Data Management Center, were used for access to waveforms, related metadata, and/or derived products used in this study. IRIS Data Services are funded through the Seismological Facilities for the Advancement of Geoscience and EarthScope (SAGE) Proposal of the National Science Foundation under Cooperative Agreement EAR-1261681. Some of the figures were generated using the mmap mapping toolbox. This work was supported by the National Science and Engineering Research Council of Canada (NSERC) Discovery Grant.

### References

- Akaogi, M., Ito, E., & Navrotsky, A. (1989). Olivine-modified spinel-spinel transitions in the system  $Mg_2SiO_4 - Fe_2SiO_4$ : Calorimetric measurements, thermochemical calculation, and geophysical application. *Journal of Geophysical Research*, 94, 15,671–15,685.
- Amaru, M. (2007). Global travel time tomography with 3-D reference models, *Geol. Traiectina* (PhD thesis). Utrecht University.
- An, Y., Gu, Y. J., & Sacchi, M. D. (2007). Imaging mantle discontinuities using least squares Radon transform. *Journal of Geophysical Research*, 112, B10303. <https://doi.org/10.1029/2007JB005009>
- Anderson, D. L. (1967). Phase changes in the upper mantle. *Science*, 157(3793), 1165–1173.
- Andrews, J., & Deuss, A. (2008). Detailed nature of the 660 km region of the mantle from global receiver function data. *Journal of Geophysical Research*, 113, B06304. <https://doi.org/10.1029/2007JB005111>
- Bassin, C. (2000). The current limits of resolution for surface wave tomography in North America. *Eos, Transactions American Geophysical Union*, 81, F897.
- Baysal, E., Kosloff, D. D., & Sherwood, J. W. (1983). Reverse time migration. *Geophysics*, 48(11), 1514–1524.
- Bijwaard, H., Spakman, W., & Engdahl, E. R. (1998). Closing the gap between regional and global travel time tomography. *Journal of Geophysical Research*, 103, 30,055–30,078.
- Biondi, B., & Shan, G. (2002). Prestack imaging of overturned reflections by reverse time migration. In *SEG Technical Program Expanded Abstracts* (Vol. 21, pp. 1284–1287).
- Bird, P. (2003). An updated digital model of plate boundaries. *Geochemistry, Geophysics, Geosystems*, 4(3), 1027. <https://doi.org/10.1029/2001GC000252>
- Bock, Y., Prawirodirdjo, L., Genrich, J. F., Stevens, C. W., McCaffrey, R., Subarya, C., ... Calais, E. (2003). Crustal motion in Indonesia from global positioning system measurements. *Journal of Geophysical Research*, 108(B8), 2367. <https://doi.org/10.1029/2001JB000324>
- Braña, L., & Helffrich, G. (2004). A scattering region near the core-mantle boundary under the North Atlantic. *Geophysical Journal International*, 158(2), 625–636.
- Cao, Q., Wang, P., Van der Hilst, R. D., De Hoop, M. V., & Shim, S.-H. (2010). Imaging the upper mantle transition zone with a generalized Radon transform of SS precursors. *Physics of the Earth and Planetary Interiors*, 180(1), 80–91.
- Cardwell, R. K., & Isacks, B. L. (1978). Geometry of the subducted lithosphere beneath the Banda Sea in eastern Indonesia from seismicity and fault plane solutions. *Journal of Geophysical Research*, 83(B6), 2825–2838.
- Chang, W.-F., & McMechan, G. A. (1994). 3-D elastic prestack, reverse-time depth migration. *Geophysics*, 59(4), 597–609.
- Claerbout, J. F., & Doherty, S. M. (1972). Downward continuation of moveout-corrected seismograms. *Geophysics*, 37(5), 741–768.
- Curry, J. R., Moore, D. G., Lawyer, L. A., Emmel, F. J., Raitt, R. W., Henry, M., & Kieckhefer, R. (1979). Tectonics of the Andaman Sea and Burma: Convergent margins. *AAPG Special Volumes*, 29, 189–198.
- Dahlen, F. A. (2005). Finite-frequency sensitivity kernels for boundary topography perturbations. *Geophysical Journal International*, 162(2), 525–540.
- DeMets, C., Gordon, R. G., & Argus, D. F. (2010). Geologically current plate motions. *Geophysical Journal International*, 181(1), 1–80.
- Deuss, A. (2009). Global observations of mantle discontinuities using SS and PP precursors. *Surveys in Geophysics*, 30(4–5), 301–326.
- Dokht, R. M., Gu, Y. J., & Sacchi, M. D. (2016). Waveform inversion of SS precursors: An investigation of the northwestern Pacific subduction zones and intraplate volcanoes in China. *Gondwana Research*, 40, 77–90.
- Dziewonski, A. M., & Anderson, D. L. (1981). Preliminary reference Earth model. *Physics of the Earth and Planetary Interiors*, 25(4), 297–356.
- Edwards, C. M., Menzies, M. A., Thirwall, M. F., Morris, J. D., Leeman, W. P., & Harmon, R. S. (1994). The transition to potassic alkaline volcanism in island arcs: The Ringgit-Beser complex, East Java, Indonesia. *Journal of Petrology*, 35(6), 1557–1595.
- Efron, B., & Tibshirani, R. (1991). Statistical data analysis in the computer age. *Science*, 253(5018), 390–395.
- Etgen, J., Gray, S. H., & Zhang, Y. (2009). An overview of depth imaging in exploration geophysics. *Geophysics*, 74(6), WCA5–WCA17.
- Fichtner, A., De Wit, M., & van Bergen, M. (2010). Subduction of continental lithosphere in the Banda Sea region: Combining evidence from full waveform tomography and isotope ratios. *Earth and Planetary Science Letters*, 297(3), 405–412.
- Flanagan, M. P., & Shearer, P. M. (1998). Global mapping of topography on transition zone velocity discontinuities by stacking SS precursors. *Journal of Geophysical Research*, 103(B2), 2673–2692.
- Frederiksen, A. W., & Revenaugh, J. (2004). Lithospheric imaging via teleseismic scattering tomography. *Geophysical Journal International*, 159(3), 978–990.
- Fukao, Y., & Obayashi, M. (2013). Subducted slabs stagnant above, penetrating through, and trapped below the 660 km discontinuity. *Journal of Geophysical Research: Solid Earth*, 118, 5920–5938. <https://doi.org/10.1002/2013JB010466>
- Fukao, Y., Obayashi, M., Inoue, H., & Nenbai, M. (1992). Subducting slabs stagnant in the mantle transition zone. *Journal of Geophysical Research*, 97(B4), 4809–4822.
- Gazdag, J. (1978). Wave equation migration with the phase-shift method. *Geophysics*, 43(7), 1342–1351.
- Gazdag, J., & Sguazzero, P. (1984). Migration of seismic data. *Proceedings of the IEEE*, 72(10), 1302–1315.
- Gorbato, A., & Kennett, B. L. N. (2003). Joint bulk-sound and shear tomography for Western Pacific subduction zones. *Earth and Planetary Science Letters*, 210(3), 527–543.
- Gossler, J., & Kind, R. (1996). Seismic evidence for very deep roots of continents. *Earth and Planetary Science Letters*, 138(1), 1–13.
- Grand, S. P. (2002). Mantle shear-wave tomography and the fate of subducted slabs. *Philosophical Transactions of the Royal Society of London A: Mathematical, Physical and Engineering Sciences*, 360(1800), 2475–2491.
- Gray, S. H., Etgen, J., Dellinger, J., & Whitmore, D. (2001). Seismic migration problems and solutions. *Geophysics*, 66(5), 1622–1640.
- Gu, Y., Dziewonski, A. M., & Agee, C. B. (1998). Global de-correlation of the topography of transition zone discontinuities. *Earth and Planetary Science Letters*, 157(1), 57–67.
- Gu, Y. J., & Dziewonski, A. M. (2002). Global variability of transition zone thickness. *Journal of Geophysical Research*, 107(B7), 2135. <https://doi.org/10.1029/2001JB000489>
- Gu, Y. J., Dziewoński, A. M., & Ekström, G. (2003). Simultaneous inversion for mantle shear velocity and topography of transition zone discontinuities. *Geophysical Journal International*, 154(2), 559–583.
- Gu, Y. J., Okeler, A., & Schultz, R. (2012). Tracking slabs beneath northwestern Pacific subduction zones. *Earth and Planetary Science Letters*, 331, 269–280.
- Hall, R., & Spakman, W. (2015). Mantle structure and tectonic history of SE Asia. *Tectonophysics*, 658, 14–45.

- Hall, R., Cross, L., Clements, B., & Spakman, W. (2009). Neogene subduction beneath Java: Slab tearing, arc deformation and arc magmatism, and their causes. In *Southeast Asian Gateway Evolution Conference (Abstract)*, Royal Holloway University of London, United Kingdom.
- Hamilton, W. B. (1974). Earthquake map of the Indonesian region (Tech. Rep.) USGS Map I-875C, 1:5,000,000.
- Hanitzsch, C. (1997). Comparison of weights in prestack amplitude-preserving Kirchhoff depth migration. *Geophysics*, 62(6), 1812–1816.
- Hayes, G. P., Wald, D. J., & Johnson, R. L. (2012). Slab1.0: A three-dimensional model of global subduction zone geometries. *Journal of Geophysical Research*, 117, B01302. <https://doi.org/10.1029/2011JB008524>
- Honda, S., Morishige, M., & Orihashi, Y. (2007). Sinking hot anomaly trapped at the 410 km discontinuity near the Honshu subduction zone, Japan. *Earth and Planetary Science Letters*, 261(3), 565–577.
- Houser, C., Masters, G., Flanagan, M., & Shearer, P. (2008). Determination and analysis of long-wavelength transition zone structure using SS precursors. *Geophysical Journal International*, 174(1), 178–194.
- Houser, C., & Williams, Q. (2010). Reconciling Pacific 410 and 660 km discontinuity topography, transition zone shear velocity patterns, and mantle phase transitions. *Earth and Planetary Science Letters*, 296(3), 255–266.
- Huang, Z., Zhao, D., & Wang, L. (2015). P wave tomography and anisotropy beneath Southeast Asia: Insight into mantle dynamics. *Journal of Geophysical Research: Solid Earth*, 120, 5154–5174. <https://doi.org/10.1002/2015JB012098>
- IRIS, DMC (2013). Data services products. SEMum, a high-resolution global model of upper mantle structure. <https://doi.org/10.17611/DP/9991866>
- Ito, E., & Takahashi, E. (1989). Postspinel transformations in the system  $Mg_2SiO_4$ – $Fe_2SiO_4$  and some geophysical implications. *Journal of Geophysical Research*, 94(B8), 10,637–10,646.
- Jeanloz, R., & Thompson, A. B. (1983). Phase transitions and mantle discontinuities. *Reviews of Geophysics*, 21(1), 51–74.
- Katili, J. A. (1975). Volcanism and plate tectonics in the Indonesian island arcs. *Tectonophysics*, 26(3–4), 165–188.
- Katsura, T., & Ito, E. (1989). The system  $Mg_2SiO_4$ – $Fe_2SiO_4$  at high pressures and temperatures: Precise determination of stabilities of olivine, modified spinel, and spinel. *Journal of Geophysical Research*, 94(B11), 15,663–15,670.
- Kazemi, N., & Siahkoohi, H. R. (2012). Local stretch zeroing NMO correction. *Geophysical Journal International*, 188(1), 123–130.
- Kühl, H., & Sacchi, M. D. (2003). Least-squares wave-equation migration for AVP/AVA inversion. *Geophysics*, 68(1), 262–273.
- Lawrence, J. F., & Shearer, P. M. (2006). A global study of transition zone thickness using receiver functions. *Journal of Geophysical Research*, 111, B06307. <https://doi.org/10.1029/2005JB003973>
- Lawrence, J. F., & Shearer, P. M. (2008). Imaging mantle transition zone thickness with SdS-SS finite-frequency sensitivity kernels. *Geophysical Journal International*, 174(1), 143–158.
- Lekić, V., & Romanowicz, B. (2011). Inferring upper-mantle structure by full waveform tomography with the spectral element method. *Geophysical Journal International*, 185(2), 799–831.
- Lessing, S., Thomas, C., Rost, S., Cobden, L., & Dobson, D. P. (2014). Mantle transition zone structure beneath India and Western China from migration of PP and SS precursors. *Geophysical Journal International*, 197(1), 396–413.
- Lessing, S., Thomas, C., Saki, M., Schmerr, N., & Vanacore, E. (2015). On the difficulties of detecting PP precursors. *Geophysical Journal International*, 201(3), 1666–1681.
- Li, X., & Yuan, X. (2003). Receiver functions in northeast China—Implications for slab penetration into the lower mantle in northwest Pacific subduction zone. *Earth and Planetary Science Letters*, 216(4), 679–691.
- Long, M. D., & Silver, P. G. (2008). The subduction zone flow field from seismic anisotropy: A global view. *Science*, 319(5861), 315–318.
- Minster, J. B., & Jordan, T. H. (1978). Present-day plate motions. *Journal of Geophysical Research*, 83(B11), 5331–5354.
- Morishige, M., Honda, S., & Yoshida, M. (2010). Possibility of hot anomaly in the sub-slab mantle as an origin of low seismic velocity anomaly under the subducting Pacific plate. *Physics of the Earth and Planetary Interiors*, 183(1), 353–365.
- Neale, F., de Regt, H., & Van Decar, J. (1997). Gross errors in upper-mantle discontinuity topography from underside reflection data. *Geophysical Journal International*, 129(1), 194–204.
- Niu, Y. L. (2014). Geological understanding of plate tectonics: Basic concepts, illustrations, examples and new perspectives. *Global Tectonics and Metallogenesis*, 10(1), 23–46.
- Obayashi, M., Sugioka, H., Yoshimitsu, J., & Fukao, Y. (2006). High temperature anomalies oceanward of subducting slabs at the 410-km discontinuity. *Earth and Planetary Science Letters*, 243(1), 149–158.
- Phipps Morgan, J., Hasenlever, J., Hort, M., Rüpkne, L., & Parmentier, E. M. (2007). On subducting slab entrainment of buoyant asthenosphere. *Terra Nova*, 19(3), 167–173.
- Piazzoni, A. S., Steinle-Neumann, G., Bunge, H.-P., & Dolejš, D. (2007). A mineralogical model for density and elasticity of the Earth's mantle. *Geochemistry, Geophysics, Geosystems*, 8, Q11010. <https://doi.org/10.1029/2007GC001697>
- Puspito, N. T., & Shimazaki, K. (1995). Mantle structure and seismotectonics of the Sunda and Banda arcs. *Tectonophysics*, 251(1), 215–228.
- Puspito, N. T., Yamanaka, Y., Miyatake, T., Shimazaki, K., & Hirahara, K. (1993). Three-dimensional P-wave velocity structure beneath the Indonesian region. *Tectonophysics*, 220(1), 175–192.
- Replumaz, A., Kárasón, H., van der Hilst, R. D., Besse, J., & Tapponnier, P. (2004). 4-D evolution of SE Asia's mantle from geological reconstructions and seismic tomography. *Earth and Planetary Science Letters*, 221(1), 103–115.
- Ritsema, J., van Heijst, H. J., & Woodhouse, J. H. (1999). Complex shear wave velocity structure imaged beneath Africa and Iceland. *Science*, 286(5446), 1925–1928.
- Rost, S., & Thomas, C. (2009). Improving seismic resolution through array processing techniques. *Surveys in Geophysics*, 30(4–5), 271–299.
- Saita, T., Suetsugu, D., Ohtaki, T., Takenaka, H., Kanjo, K., & Purwana, I. (2002). Transition zone thickness beneath Indonesia as inferred using the receiver function method for data from the JISNET regional broadband seismic network. *Geophysical Research Letters*, 29(7), 1115. <https://doi.org/10.1029/2001GL013629>
- Schmerr, N., & Garnero, E. (2006). Investigation of upper mantle discontinuity structure beneath the central Pacific using SS precursors. *Journal of Geophysical Research*, 111, B08305. <https://doi.org/10.1029/2005JB004197>
- Schmerr, N., & Thomas, C. (2011). Subducted lithosphere beneath the Kuriles from migration of PP precursors. *Earth and Planetary Science Letters*, 311(1), 101–111.
- Schneider, W. A. (1978). Integral formulation for migration in 2 and 3 dimensions. *Geophysics*, 43(1), 49–76.
- Schlitz, R., & Gu, Y. J. (2013). Multiresolution imaging of mantle reflectivity structure using SS and  $P'$   $P''$  precursors. *Geophysical Journal International*, 195(1), 668–683.
- Shearer, P. M. (1993). Global mapping of upper mantle reflectors from long-period SS precursors. *Geophysical Journal International*, 115(3), 878–904.
- Shearer, P. M., Flanagan, M. P., & Hedlin, M. A. (1999). Experiments in migration processing of SS precursor data to image upper mantle discontinuity structure. *Journal of Geophysical Research*, 104(B4), 7229–7242.
- Sheriff, R. E., & Geldart, L. P. (1995). *Exploration seismology*. Cambridge, UK: Cambridge University Press.

- Simmons, N. A., Forte, A. M., & Grand, S. P. (2007). Thermochemical structure and dynamics of the African superplume. *Geophysical Research Letters*, 34, L02301. <https://doi.org/10.1029/2006GL028009>
- Simons, W. J. F., Socquet, A., Vigny, C., Ambrosius, B. A. C., Haji Abu, S., Promthong, C., ... Spakman, W. (2007). A decade of GPS in Southeast Asia: Resolving Sundaland motion and boundaries. *Journal of Geophysical Research*, 112, B06420. <https://doi.org/10.1029/2005JB003868>
- Spakman, W., & Hall, R. (2010). Surface deformation and slab-mantle interaction during Banda arc subduction rollback. *Nature Geoscience*, 3(8), 562–566.
- Stixrude, L., & Lithgow-Bertelloni, C. (2005). Thermodynamics of mantle minerals—I. Physical properties. *Geophysical Journal International*, 162(2), 610–632.
- Tajima, F., & Grand, S. P. (1995). Evidence of high velocity anomalies in the transition zone associated with southern Kurile subduction zone. *Geophysical Research Letters*, 22(23), 3139–3142.
- Thomas, C., & Billen, M. I. (2009). Mantle transition zone structure along a profile in the SW Pacific: Thermal and compositional variations. *Geophysical Journal International*, 176(1), 113–125.
- Thomas, C., Kendall, J.-M., & Lowman, J. (2004). Lower-mantle seismic discontinuities and the thermal morphology of subducted slabs. *Earth and Planetary Science Letters*, 225(1), 105–113.
- Wang, T., & Chen, L. (2009). Distinct velocity variations around the base of the upper mantle beneath northeast Asia. *Physics of the Earth and Planetary Interiors*, 172(3), 241–256.
- Weidner, D. J., & Wang, Y. (1998). Chemical-and Clapeyron-induced buoyancy at the 660 km discontinuity. *Journal of Geophysical Research*, 103(134), 7431–7441.
- Widiyantoro, S., & van der Hilst, R. (1996). Structure and evolution of lithospheric slab beneath the Sunda arc, Indonesia. *Science*, 271(5255), 1566–1570.
- Widiyantoro, S., & van der Hilst, R. (1997). Mantle structure beneath Indonesia inferred from high-resolution tomographic imaging. *Geophysical Journal International*, 130(1), 167–182.
- Widiyantoro, S., Pesicek, J. D., & Thurber, C. H. (2011a). Subducting slab structure below the eastern Sunda arc inferred from non-linear seismic tomographic imaging. *Geological Society, London, Special Publications*, 355(1), 139–155.
- Widiyantoro, S., Pesicek, J. D., & Thurber, C. H. (2011b). Complex structure of the lithospheric slab beneath the Banda arc, eastern Indonesia depicted by a seismic tomographic model. *Research in Geophysics*, 7(1), 1.
- Yu, Y., Zhao, D., & Lei, J. (2017). Mantle transition zone discontinuities beneath the Tien Shan. *Geophysical Journal International*, 211(1), 80–92.
- Zhang, H., Ni, S., Chu, R., & Schmandt, B. (2017). An algorithm for computing synthetic body waves due to underside conversion on an undulating interface and application to the 410 km discontinuity. *Geophysical Journal International*, 210(3), 1858–1871.
- Zhao, D., Maruyama, S., & Omori, S. (2007). Mantle dynamics of Western Pacific and East Asia: insight from seismic tomography and mineral physics. *Gondwana Research*, 11(1), 120–131.
- Zhao, L., & Chevrot, S. (2003). SS-wave sensitivity to upper mantle structure: Implications for the mapping of transition zone discontinuity topographies. *Geophysical Research Letters*, 30(11), 1590. <https://doi.org/10.1029/2003GL017223>
- Zheng, Z., Ventosa, S., & Romanowicz, B. (2015). High resolution upper mantle discontinuity images across the Pacific Ocean from SS precursors using local slant stack filters. *Geophysical Journal International*, 202(1), 175–189.